

Computational Screening of Anode Coatings for Garnet-Type Solid-State Batteries

Chencheng Liu,^[a] Herbert Früchtl,^[a] John T. S. Irvine,^[a] and Michael Bühl*^[a]

Making use of a large materials database of DFT-derived structures and energies, we applied a high-throughput computational screening framework to identify lithium-containing oxides as potential anode coatings for lithium (Li) garnet. A preselection of candidate materials was made based on their phase stability, electrochemical stability, and chemical stability, as emerging from this database. Then first-principles calculations (periodic DFT calculations at the PBE level) were performed to further evaluate the Li-ion conductivity and Li wettability of these coatings. A total of 10 Li–M–O compounds

(Li_3BO_3 , LiAlO_2 , Li_5AlO_4 , Li_4SiO_4 , Li_8SiO_6 , Li_4TiO_4 , Li_8TiO_6 , $\text{Li}_6\text{Zr}_2\text{O}_7$, Li_2HfO_3 and $\text{Li}_6\text{Hf}_2\text{O}_7$) were identified as the most promising anode coatings. According to our findings, lithium concentration can affect the desired electrochemical stability and Li wettability in an opposing way. Compounds with high Li content tend to have low reduction potential with poor lithium wettability. Target materials may have a “sweet spot” in terms of Li content, where all key properties are balanced in an optimal way.

Introduction

Rechargeable lithium-ion (Li-ion) batteries have enabled the revolution of the portable electronics industry in the past decades. However, with the increasing demands for high-performance applications such as electric vehicles and grid-level storage systems, current Li-ion battery technology has almost approached its limit. Therefore, development beyond Li-ion technology is needed for high energy density batteries. All-solid-state batteries provide a promising solution for the problems encountered in traditional Li-ion batteries. By replacing organic liquid electrolytes with inorganic solid-state electrolytes (SSEs), all-solid-state batteries often show higher electrochemical stability and safety. In addition, directly using Li metal as anode enables them to achieve high energy density.^[1–4] To date, various structural families in SSEs have been investigated, including oxides (LISICON^[5] and NASICON^[6] type Li-ion conductors, perovskites,^[7] garnets^[8]), sulfides (thio-LISICONs,^[9] LGPS,^[10] glassy-type $\text{Li}_2\text{S}-\text{P}_2\text{S}_5$ ^[11]), argyrodites^[12] and others.

Among all the different types of SSEs, garnet-type $\text{Li}_7\text{La}_3\text{Zr}_2\text{O}_{12}$ (LLZO) SSE shows the most attractive properties in terms of high ionic conductivity,^[13–15] a wide electrochemical stability window, good stability against Li metal, and environmental stability during the process.^[16–18] However, the high interfacial resistance between electrodes and electrolytes is the main challenge for commercial applications. On the anode side,

the high interfacial resistance is due to the poor physical contact between Li metal and the garnet. Several studies point out that the poor contact can be caused by either poor adhesion or the presence of impurities on the garnet surface.^[19] Different strategies have been proposed to reduce the Li/LLZO interfacial resistance. One of those strategies is surface modification, which aims to remove the surface impurities on the garnet surface, such as Li_2CO_3 and LiOH . Through physical polishing of Al-doped LLZO, a low interfacial area specific resistance of $109 \Omega \text{cm}^2$ was achieved.^[20] Wet polishing the garnet surface can further reduce the interfacial resistance to $2 \Omega \text{cm}^2$.^[21] Other surface modification methods have also been investigated, including chemical treatment^[22,23] and thermal decomposition.^[24,25] Applying an artificial interlayer on the garnet surface is another strategy to reduce the interfacial resistance by increasing the wettability towards lithium metal. For example, the addition of alloy elements such as Al, Au, Ag, Cu, Ge and Si has successfully reduced the interfacial resistance to $9.8\text{--}127 \Omega \text{cm}^2$.^[26–31] Other coating materials such as ZnO and Al_2O_3 can also increase the lithium wettability by reacting with molten Li.^[32,33] In one case, the interfacial resistance has been reported to be reduced to $1 \Omega \text{cm}^2$ through atomic layer deposition of Al_2O_3 .^[33]

However, the development of new coating materials using a purely experimental approach highly relies on trial and error. To alleviate this, high-throughput computational screening methods have been developed to find suitable cathode coating materials.^[34,35] Nolan et al. studied the chemical and electrochemical stability of Li–M–O cathode coatings with both garnet electrolyte and NMC cathode based on thermodynamic analyses.^[36] Chen et al. investigated the electrochemical stability windows and migration barriers of Mg binary and ternary compounds to identify anode coating candidates for Mg batteries.^[37,38] Honrao et al. used machine-learning techniques to predict migration barriers and oxidation and reduction potentials in order to design novel solid electrolytes and anode

[a] C. Liu, Dr. H. Früchtl, Prof. J. T. S. Irvine, Prof. M. Bühl

School of Chemistry

University of St Andrews

North Haugh, St Andrews, Fife KY16 9ST, United Kingdom

E-mail: buehl@st-andrews.ac.uk

 Supporting information for this article is available on the WWW under <https://doi.org/10.1002/batt.202100357>

 © 2022 The Authors. *Batteries & Supercaps* published by Wiley-VCH GmbH. This is an open access article under the terms of the Creative Commons Attribution License, which permits use, distribution and reproduction in any medium, provided the original work is properly cited.

coatings.^[39] To the best of our knowledge, the evaluation of wettability has not been included routinely in this screening framework. In this study, we systematically investigate what we believe to be key properties, namely phase stability, electrochemical stability, chemical stability, Li-ion conductivity and Li wettability, in order to identify ideal anode coating materials for garnet-type all-solid-state batteries. Because oxide coating has achieved great success in reducing the resistance across the Li/LLZO interface, we hereby limit our screening to Li–M–O lithium ternary oxides. By combining a high-throughput screening framework and first-principles calculations, we intend to provide a comprehensive understanding of new anode coating materials which can be used for the development of garnet-type all-solid-state batteries.

Results and Discussion

Owing to the large number of possible materials, we limited the screening to Li–M–O lithium ternary oxides because most notable SSEs reported in the literature contain lithium sub-lattices, which enable reasonable Li-ion conductivity. Compounds with Kohn-Sham band gaps (E_g) of less than 0.5 eV were subsequently excluded to ensure that no electronic conductors are among the candidates. A total of 951 compounds were collected from the Materials Project (MP) database.^[40] Our screening strategy involved five important properties for suitable anode coating application: a) phase stability, b) electrochemical stability, c) chemical stability, d) Li-ion conductivity, e) Li wettability. Figure 1 presents the framework of computational screening for Li–M–O anode coatings.

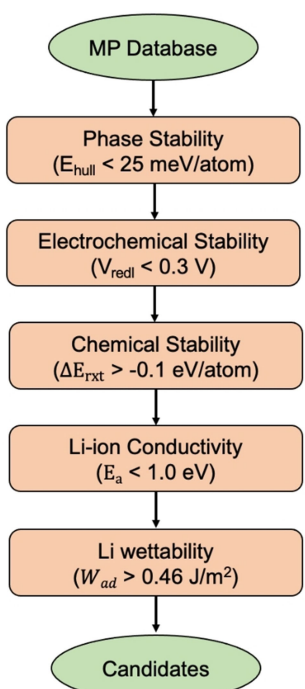


Figure 1. Computational screening framework for Li–M–O anode coating candidates based on different screening criteria.

Phase stability screening

The first step of our screening process is phase stability screening. A promising coating is expected to be stable against decomposition during operation. The phase stability of each material was analysed using the convex hull method (see Experimental Section). In general, materials with an energy that lies on the convex hull are considered to be thermodynamically stable at 0 K and amenable to synthesis at room temperature. Considering entropic contributions and metastable phases, we also included materials with energy above the convex hull < 0.025 eV/atom.^[41] A total of 296 compounds passed the phase stability filter and were accepted for further evaluation.

Electrochemical stability screening

For the second step, the electrochemical stability of each material was evaluated by constructing its related grand potential phase diagram and the stability window. Note that the equilibrium values from the grand potential phase are based on thermodynamic quantities. In reality, some kinetic stabilisation may occur (e.g., through overpotentials), which can be considered in this model by adjusting the acceptable stability window. On the anode side, the reduction limit should ideally be 0 V to prevent any decomposition in contact with Li metal. In this study, materials with reduction potential up to +0.3 V are included allowing potential kinetic stabilisation. This value was chosen based on a study of Li₃BO₃ coatings, where it was observed that Li₃BO₃ is unreactive with a Li metal anode even though the predicted reduction potential is 0.29 eV.^[41,42] Figure 2 shows a representative example of the calculated phase diagram and the stability window for Li–Al–O compounds. Compounds with chemical composition LiAl₅O₈, LiAlO₂ and Li₅AlO₄ are the most stable phases where the energy above the convex hull equals 0 eV/atom. Compound LiAl₅O₈ was subsequently excluded due to the high reduction potential of 0.79 V. After excluding lanthanides and actinides, similar phase diagrams were constructed for other elements M in the ternary Li–M–O systems. We identified 13 compounds that passed the electrochemical stability filter. Figure 3 shows the stability window for all 13 compounds, as well as the LLZO garnet electrolyte. The calculated reduction and oxidation potentials for all compounds are listed in Table S1.

The calculated electrochemical stability window of the LLZO is 0.03 to 3.16 V versus Li/Li⁺, which is in agreement with another computational study (0.05 to 2.91 V).^[43] All anode coating candidates shown in Figure 3 exhibit a wide stability window (from 2.6 to 3.5 V), which implies good electrochemical stability. The Li–Hf–O compounds exhibit overall the lowest reduction potential among all coating candidates. The reduction potential of Li₆Hf₂O₇ and Li₈HfO₆ can be as low as 0 V, which is ideal for anode coatings. However, Li₂HfO₃ has a higher reduction potential of 0.13 V, which confirms Siegel's finding that Li-rich compounds normally have lower reduction potential than Li-deficient ones.^[41] Li₅AlO₄ also has a low reduction potential of 0.01 V, indicating a promising anode

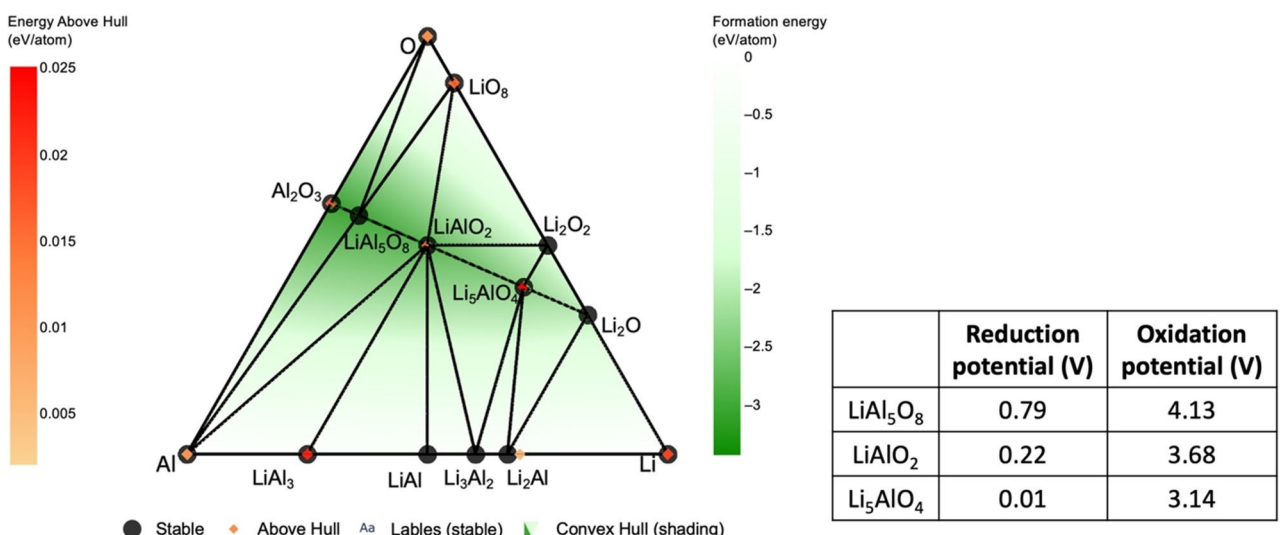


Figure 2. Phase diagram and the calculated reduction and oxidation potentials of Li–Al–O compounds (i.e., the $[\mu_{\text{ox}}, \mu_{\text{red}}]$ range over which the compound is computed to be stable).

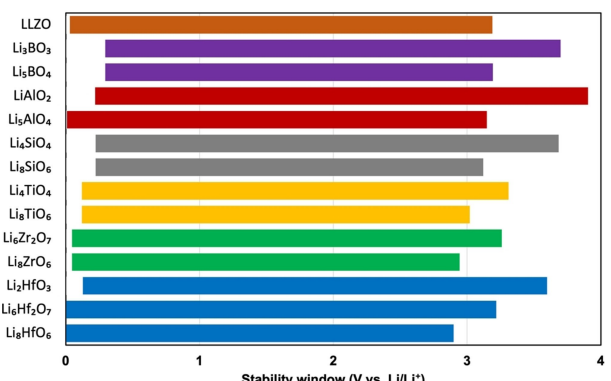


Figure 3. Electrochemical stability window of all Li–M–O compounds.

coating. The slightly higher reduction potential of 0.22 V in LiAlO_2 probably results from its low Li content. For Li-rich compounds, the reduction potential shows an increasing trend in Li–Zr–O, Li–Ti–O and Li–Si–O compounds, with a reduction potential of 0.05, 0.12 and 0.22 V, respectively. The Li–B–O compounds have the highest reduction potential of 0.29 V, implying less electrochemical stability at low voltage.

Chemical stability screening

A good anode coating material is also expected to be chemically stable when it is in contact with electrolyte and anode. For the next step, we calculated the driving force for the chemical mixing reaction between our coating candidates and both LLZO electrolyte and a Li metal anode. Only materials with a chemical mixing reaction energy $\Delta E_{\text{rx}} > -0.1$ eV/atom passed the chemical stability filter. From a purely thermodynamic point of view, this should be ≥ 0 (or rather zero in our approach, where we minimise this quantity with respect to the

product composition; see computational details). However, compounds that are unstable thermodynamically can be very long-lived because of high kinetic barriers for decomposition. In general, the higher the driving force for a reaction (i.e., the more negative the reaction free energy), the lower the activation barrier tends to be. We picked the threshold of -0.1 eV/atom as a conservative estimate for a reaction that is only mildly favourable, and for which a sizeable kinetic barrier is to be expected. As shown in Table 1, the maximum reaction energy between coating candidates and LLZO is equal to their energy above the convex hull of the coatings themselves. The largest driving force of the chemical mixing reaction happens when the LLZO mixing ratio is 0, which implies an excellent chemical stability between the LLZO electrolyte and all anode coating candidates.

Table 1 also shows the maximum chemical mixing reaction energy between the coating candidates and Li metal anode (see Table S2 for the resulting mixing ratio according to Equation (3) from Experimental Section). Li–Hf–O compounds showed overall good chemical stability against Li metal anode with a reaction energy range from -0.011 to 0 eV/atom. Li_5AlO_4 , Li–Zr–O and Li–Ti–O compounds are also chemically stable against an Li metal anode with a reaction energy range from -0.033 to -0.003 eV/atom. The reaction energies in LiAlO_2 , Li–Si–O and Li–B–O compounds range from -0.098 to -0.076 eV/atom, indicating less chemical stability compared to other coating candidates. Nevertheless, all 13 compounds that passed the electrochemical stability filter have small chemical mixing energy with both LLZO electrolyte and Li metal anode.

Li-ion conductivity screening

So far, our screening protocol has made use of the data from the MP database. We now turn to the Li-ion conductivity and Li wettability criteria (cf. Figure 1), for which additional DFT

Table 1. Chemical mixing reaction energy between coatings and LLZO electrolyte.

Coatings	MP ID	E_{hull} [eV/atom]	ΔE_{rxn} with LLZO [eV/atom]	ΔE_{rxn} with Li [eV/atom]
Li_3BO_3	mp-27275	0	0	-0.095
Li_5BO_4	mp-768960	0.024	-0.024	-0.098
LiAlO_2	mp-3427	0	0	-0.079
Li_5AlO_4	mp-15960	0	0	-0.003
Li_4SiO_4	mp-1223129	0	0	-0.098
Li_8SiO_6	mp-28549	0.005	-0.005	-0.076
Li_4TiO_4	mp-9172	0	0	-0.033
Li_8TiO_6	mp-772521	0.004	-0.004	-0.025
$\text{Li}_6\text{Zr}_2\text{O}_7$	mp-5418	0	0	-0.015
Li_8ZrO_6	mp-755225	0.001	-0.001	-0.009
Li_2HfO_3	mp-755352	0	0	-0.011
$\text{Li}_6\text{Hf}_2\text{O}_7$	mp-772185	0	0	0
Li_8HfO_6	mp-752922	0.003	-0.003	-0.003

calculations are necessary. Li-ion transport is important for Li electrodeposition. Studies have found that coatings with high Li-ion conductivity can not only improve the cell performance^[44] but also suppress Li dendrite growth.^[45] The Li-ion migration mechanism for each compound was assessed following the methodology used by Zhang and coworkers.^[46] The less accurate bond-valence (BV) method was first used to find a reasonable Li-ion migration pathway using the PyAb-stacia program.^[47] Then a more precise DFT calculation was performed using the CI-NEB method to evaluate the Li-ion vacancy migration barriers. Materials with a small migration barrier are expected to have high Li-ion conductivity at room temperature. Figure 4 shows an example of the Li-ion migration pathway in the *ab* plane in LiAlO_2 as well as the migration barriers.

In each structure, we considered two possible vacancy hopping pathways in different directions roughly perpendicular to each other. Since all structures at this point are at least tetragonal, we chose one hopping event roughly within the *ab*

plane and one roughly along the *c* axis (the precise direction will depend on the particular crystal structure). In most cases, a single hopping event should be sufficient to describe migration through the bulk due to symmetry. Where this is not the case, we chose two representative hopping events (see Figure S1 for the pathways that have been traced). It is also possible that migration of interstitial Li atoms, rather than of vacancies can contribute to the overall ion conductivity. For systems with low symmetry and large unit cells, complete tracing of all possible hopping pathways (including percolating paths) is a formidable task beyond the scope of the present study. We are convinced that the presence of at least one hopping pathway with a low barrier along one direction is sufficient to result in good ion conductivity (because in a real, e.g., microcrystalline material, continuous pathways through the material can be constructed along the preferred directions in each crystallite). A common, conservative threshold for migration barriers in good Li-ion conductors would be less than 0.5 eV. However, the maximum tolerable migration barrier can be tuned by the thickness of the coating, the (dis)charge rate and the temperature. If the coating can be made on the nanometre scale, a higher migration barrier can be tolerated.^[38] Thus, we slightly relaxed the criterion to 1 eV in our screening procedure, allowing for such variable operation conditions. The lowest calculated Li-ion migration barriers for all 13 compounds are listed in Table 2 (the full set of barriers is collected in Table S3). The minimum migration barrier of Li_3BO_3 is calculated to be 0.86 eV, with a

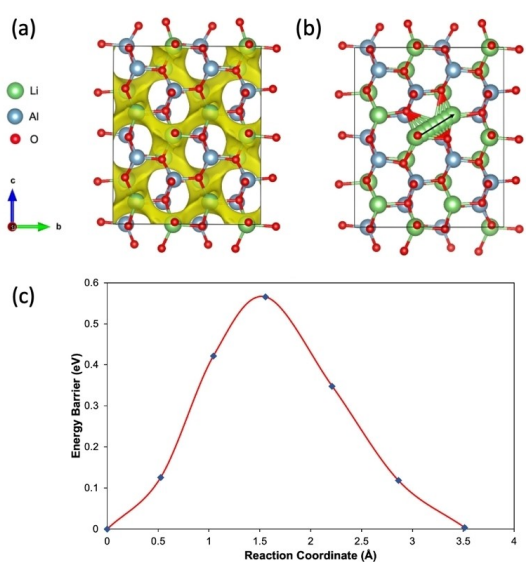


Figure 4. a) Calculated Li-ion migration pathway for LiAlO_2 using the bond-valence sum map method. b) Selected Li-ion migration along the *ab* plane. c) Calculated migration energy barrier for LiAlO_2 using the CI-NEB method.

Table 2. Minimum Li-ion migration barrier for all coating candidates.

Coating	Minimum migration barrier [eV]
Li_3BO_3	0.86
Li_5BO_4	0.33
LiAlO_2	0.57
Li_5AlO_4	0.52
Li_4SiO_4	0.63
Li_8SiO_6	0.44
Li_4TiO_4	0.51
Li_8TiO_6	0.39
$\text{Li}_6\text{Zr}_2\text{O}_7$	0.79
Li_8ZrO_6	0.56
Li_2HfO_3	0.66
$\text{Li}_6\text{Hf}_2\text{O}_7$	0.65
Li_8HfO_6	0.59

relatively high room-temperature ionic conductivity of $2 \times 10^{-6} \text{ S cm}^{-1}$ measured by experimental study.^[48] The migration barrier of 0.33 eV implies that Li_5BO_4 has a significantly higher Li-ion conductivity than Li_3BO_3 . The calculated migration barrier for LiAlO_2 is 0.57 eV, which shows good agreement with other computational studies (0.57 eV using CI-NEB method^[49] and 0.56 eV using AIMD simulation^[50]). The room temperature conductivity from experimental measurement is, however, only $5.6 \times 10^{-8} \text{ S cm}^{-1}$.^[50] This difference is most likely due to the large vacancy formation energy of 5.20 eV in LiAlO_2 .^[49] The calculated minimum migration barrier for Li_5AlO_4 is 0.52 eV. This is consistent with another computational study finding 0.49 eV using the bond valence method.^[51] The small activation energy implies that Li_5AlO_4 might have a relatively high ionic conductivity at room temperature. The calculated minimum migration barrier for Li_4SiO_4 is 0.63 eV, indicating a relatively high ionic conductivity. An experimental study confirms our prediction with a conductivity of $2.5 \times 10^{-6} \text{ S cm}^{-1}$ using AC impedance measurements.^[52] The minimum migration barrier of 0.44 eV in Li_6SiO_6 suggests an even better ionic conductivity. The small migration barriers of 0.51 eV and 0.39 eV in Li_4TiO_4 and Li_8TiO_6 , respectively, imply that the Li–Ti–O system has general good ionic conductivity. Our calculated minimum migration barrier for $\text{Li}_6\text{Zr}_2\text{O}_7$, 0.79 eV, is consistent with the activation energy of 0.84 eV measured experimentally, with a relatively high conductivity of $9.4 \times 10^{-6} \text{ S/cm}$ at 300°C .^[53] Meanwhile, the low migration barrier of 0.56 eV in Li_8ZrO_6 is also expected to contribute to a high conductivity. It is worth noting that the lack of a possible pathway along the *ab* plane from BV prediction suggests a 1D ionic diffusion in both the Li_8ZrO_6 and Li_8HfO_6 crystal structures (see Table S3). The activation energy for rapid localised motion is predicted to be ~ 0.6 eV from another computational study of Li_2HfO_3 ,^[54] showing good agreement with our calculation of 0.66 eV. Similarly, the low migration barriers of 0.65 eV in $\text{Li}_6\text{Hf}_2\text{O}_7$ and 0.59 eV in Li_8HfO_6 indicate a general good conductivity in the Li–Hf–O system. Our Li-ion conductivity screening results show that all 13 coating candidates have relatively low migration barriers in at least one direction, which is expected to lead to general good conductivity.

Li wettability screening

Finally, we turn to modelling Li wettability. This is the key factor in achieving low-resistance Li–LLZO interfaces in garnet-type solid-state batteries. To evaluate the interaction between Li metal and the coating candidates, DFT calculations were performed for a coating (001) surface in contact with Li metal. The Li slab was slightly modified to accommodate the geometry of the coating slab to minimise interfacial strain. The lattice misfit and the interfacial separation of each Li-coating interface slab are listed in Table S4. Figure 5 shows an example of the atomic structure for the optimised Li– LiAlO_2 interface. Note the significant restructuring of the Li phase near the phase boundary. The surface energy of Li metal σ_{Li} is calculated to be 0.46 J/m^2 , which is consistent with a previous computa-

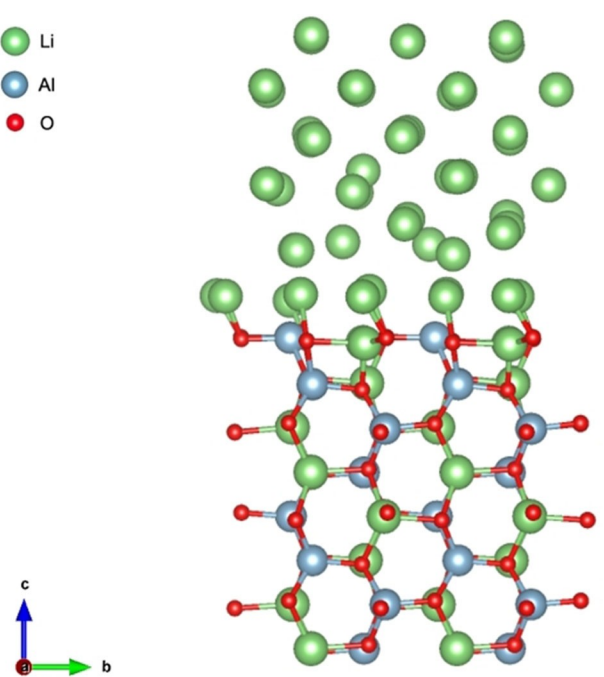


Figure 5. Interface structure calculated in the context of wetting of molten Li on a LiAlO_2 (001) surface.

tional result of 0.45 J/m^2 at essentially the same level of theory.^[21]

Table 3 shows the calculated work of adhesion and contact angles for each Li-coating interface. For comparison, we first calculated the interfacial interaction between Li metal and the LLZO garnet electrolyte (see Supporting Information for structural details). The work of adhesion is calculated to be 0.62 J/m^2 with a contact angle of 69.5° , which shows good agreement with other computational studies ($W_{\text{ad}}=0.67 \text{ J/m}^2$, $\theta=62^\circ$ and $W_{\text{ad}}=0.58 \text{ J/m}^2$, $\theta=72.8^\circ$).^[21,24] For Li–B–O compounds, the one with lowest Li content, Li_3BO_3 , shows large work of adhesion of 0.60 J/m^2 with a calculated contact angle of 72.1° , indicating that Li metal can strongly wet on Li_3BO_3 .

Table 3. Calculated work of adhesion and contact angle of Li-coating interfaces.^[a]

Interface	Work of adhesion [J/m^2]	Contact angle [$^\circ$]
Li–LLZO	0.62	69.5
Li– Li_3BO_3	0.60	72.1
Li– Li_5BO_4	0.35	104.2
Li– LiAlO_2	1.05	0
Li– Li_2AlO_4	0.59	73.3
Li– Li_4SiO_4	0.64	66.9
Li– Li_5SiO_6	0.58	75.8
Li– Li_4TiO_4	0.84	34.3
Li– Li_8TiO_6	0.55	78.2
Li– $\text{Li}_6\text{Zr}_2\text{O}_7$	0.90	17.4
Li– Li_8ZrO_6	0.23	120.0
Li– Li_2HfO_3	0.75	50.5
Li– $\text{Li}_6\text{Hf}_2\text{O}_7$	1.0	0
Li– Li_8HfO_6	0.22	120.7

[a] Highlighted in grey: compounds that do not fulfil the wettability criterion (see text).

However, the smaller work of adhesion of 0.35 J/m^2 in the Li-rich compound Li_3BO_4 indicates a weak interfacial interaction with a large contact angle of 104.2° . The same trend has also been found in $\text{Li}-\text{Al}-\text{O}$, $\text{Li}-\text{Si}-\text{O}$, $\text{Li}-\text{Ti}-\text{O}$ and $\text{Li}-\text{Zr}-\text{O}$ compounds. The large interfacial interaction of 1.05 J/m^2 in Li-poor LiAlO_2 compound indicates that Li metal can fully wet on LiAlO_2 with a contact angle of 0° . The calculated work of adhesion of 0.59 J/m^2 in the Li-rich compound Li_5AlO_4 is smaller than in LiAlO_2 (1.05 J/m^2). Nevertheless, the $\text{Li}-\text{Li}_5\text{AlO}_4$ interface also shows a strong interfacial interaction with a small wetting angle of 73.3° . For $\text{Li}-\text{Si}-\text{O}$ compounds, the calculated $W_{ad} = 0.64 \text{ J/m}^2$ in the low Li content compound Li_4SiO_4 is slightly higher than $W_{ad} = 0.58 \text{ J/m}^2$ in Li-rich Li_8SiO_6 . The contact angles are calculated to be 66.9° and 75.8° for Li_4SiO_4 and Li_8SiO_6 , respectively, meaning a general good Li wettability on $\text{Li}-\text{Si}-\text{O}$ compounds. The same phenomenon has also been found in the $\text{Li}-\text{Ti}-\text{O}$ system. The interfacial interaction in Li-deficient Li_4TiO_4 is calculated to be 0.84 J/m^2 , which is higher than the 0.55 J/m^2 in Li-rich Li_8SiO_6 . The contact angles of 34.3° and 78.2° for Li_4TiO_4 and Li_8SiO_6 , respectively, indicate that metallic Li wetting on $\text{Li}-\text{Ti}-\text{O}$ is generally good. The calculated work of adhesion is 0.90 J/m^2 in the less Li-rich $\text{Li}_6\text{Zr}_2\text{O}_7$, with a small contact angle of 17.4° , meaning that metallic Li has high wettability on $\text{Li}_6\text{Zr}_2\text{O}_7$. However, calculations on Li-rich Li_8ZrO_8 predict a small work of adhesion of 0.23 J/m^2 , with a large contact angle of 120.0° , indicating a weak Li wettability. For the $\text{Li}-\text{Hf}-\text{O}$ system, the calculated work of adhesion in Li-rich Li_8HfO_6 is 0.22 J/m^2 with a large wetting angle of 120.7° , indicating a weak interfacial interaction. The works of adhesion in the lower Li content compounds Li_2HfO_3 and $\text{Li}_6\text{Hf}_2\text{O}_7$ are predicted to be 0.75 and 1.0 J/m^2 , respectively. The contact angles of 50.0° and 0° , respectively, mean that metallic Li shows general good wettability on $\text{Li}-\text{Hf}-\text{O}$ compounds if they are not too rich in Li.

Assuming poor Li wettability when the contact angle is larger than 90° , we can exclude three compounds from the list, namely those B-, Zr- and Hf-compounds with the highest Li content (highlighted in grey in Table 3). The remaining 10 compounds (Li_3BO_3 , LiAlO_2 , Li_5AlO_4 , Li_4SiO_4 , Li_8SiO_6 , Li_4TiO_4 , Li_8TiO_6 , $\text{Li}_6\text{Zr}_2\text{O}_7$, Li_2HfO_3 and $\text{Li}_6\text{Hf}_2\text{O}_7$) have passed all our screening tests. Therefore, we propose these as "lead materials" (in analogy to lead compounds in drug discovery) for further development of anode coating materials. Those with the highest predicted Li-ion mobility (from Table 2) in this list are Li_8TiO_6 , Li_8SiO_6 , Li_4TiO_4 , Li_5AlO_4 and LiAlO_2 .

Amongst these "lead materials" we have identified, lithium aluminate is well studied, especially for its application in coating materials for Li-ion batteries. For example, coating an ultrathin LiAlO_2 layer via a sol-gel process can effectively enhance the cycling stability and rate capability of the $\text{LiNi}_{0.6}\text{Co}_{0.2}\text{Mn}_{0.2}\text{O}_2$ (NCM) cathode.^[55] Li_5AlO_4 can also be coated on an NCM cathode to improve electrochemical cycling and rate performance.^[56,57] Applying an ultrathin LiAlO_2 on the graphite anode through atomic layer deposition was found to significantly prevent the diffusion of transition metal ions from the cathode to the anode.^[50] Li_4SiO_4 is another commonly used cathode coating material in Li-ion batteries.^[58–60] Recently,

Li_4SiO_4 -based artificial layers were found to effectively suppress Li dendrite growth for lithium metal anode.^[61,62] These findings lend support to the validity and usefulness of our proposed protocol (because known coating materials have been correctly identified) and, hopefully, its predictive power. The other materials emerging from our screening have attracted comparatively less attention so far. Some of them^[63–65] have been studied for their potential use in solid breeder blankets for future fusion reactors. Our findings suggest that they could also find use in the development of new anode coatings for batteries.

Such development of real systems is likely to involve an increase in complexity beyond the rather idealised, stoichiometric materials we have studied so far. In view of this idealised nature and the many approximations inherent in our DFT computations there is always a chance that the performance of real-life materials will not fully agree with the expectations from our predictions. One way to bridge this gap is to extend the computations to larger, more complex and more realistic systems, ideally including suitable defect structures. As the number of possible minima (isomers) to explore grows with such complexity, simple geometry optimisations may not be sufficient anymore, and molecular dynamics simulations should be performed (or other multiscale methods applied). Such computations are very involved, however, and beyond the scope of the present paper.

Conclusion

In summary, we have developed a computational protocol combining a high-throughput screening approach and DFT calculations to identify promising $\text{Li}-\text{M}-\text{O}$ compounds for anode coating in garnet-type solid-state batteries. Phase stability, electrochemical stability and chemical stability were first evaluated using a high-throughput computational screening framework, using established data from a large materials database. Then, Li-ion conductivity and Li wettability were assessed based on DFT calculations. A total of 10 $\text{Li}-\text{M}-\text{O}$ compounds (Li_3BO_3 , LiAlO_2 , Li_5AlO_4 , Li_4SiO_4 , Li_8SiO_6 , Li_4TiO_4 , Li_8TiO_6 , $\text{Li}_6\text{Zr}_2\text{O}_7$, Li_2HfO_3 and $\text{Li}_6\text{Hf}_2\text{O}_7$) were found to have the most promising properties for anode coating. Especially, materials with small contact angles such as LiAlO_2 , Li_4TiO_4 , $\text{Li}_6\text{Zr}_2\text{O}_7$ and $\text{Li}_6\text{Hf}_2\text{O}_7$ are expected to achieve low interfacial resistances. Our findings also indicate that the electrochemical stability and Li wettability might be affected by the lithium concentration. For the anode side, Li-rich compounds have a general lower reduction potential (and higher Li-ion mobility) than those with lower Li content. However, according to our results, the excess Li in the coating may decrease the lithium wettability, which can lead to high interfacial resistance. Therefore, the lithium concentration needs to be carefully considered when designing new anode coating materials. Target materials may have a "sweet spot" in terms of Li content, where all key properties are balanced in an optimal way.

So far, we have applied our protocol just to ternary Li oxides with fairly simple stoichiometries (and structures).

Materials developed for use in practice tend to be more complex than that. We are confident, however, that – as additional, complementary databases are included, which can grow through characterisation of more and more complex materials – our protocol can be used for the identification of realistic “lead materials” for further optimisation (e.g., through doping).

Experimental Section

First-principles calculation

All first-principles calculations in this work were performed using density functional theory (DFT) with a plane-wave basis set and the projector augmented wave (PAW)^[66] method as implemented in the Vienna ab initio simulation package (VASP).^[67] The exchange-correlational energy was calculated using generalised gradient approximation (GGA) of the Perdew-Burke-Ernzerhof (PBE)^[68] functional. An energy cut-off of 520 eV and a k-point grid of at least 500/n_{atom} was used for all the calculations. The self-consistency convergence criterion was set to 10⁻⁵ eV and the internal atomic positions were allowed to relax until all the forces were less than 0.05 eV/Å. All the Li–M–O structures were extracted from the MP database (where they had been optimised at essentially the same level, i.e., PBE(+U) and 520 eV cutoff).

Phase stability

The Li–M–O phase diagrams were constructed using the pymatgen package^[69] to evaluate the phase equilibria of each material. The phase stability was determined by computing the energy convex hull of all known phases in the relevant phase diagram. The convex hull consists of phases with an energy lower than any other phases or linear combination of phases at the respective compositions. Only materials with an energy that lies on the convex hull are expected to be thermodynamically stable at 0 K, as materials with energy above the convex hull will decompose into their equilibrium phases.

Electrochemical stability

The electrochemical stability window of each material was obtained by constructing the lithium grand potential phase diagram, following the methodology used previously.^[43,70,71] For each considered compound, the grand potential Φ can be calculated using Equation (1):

$$\Phi[c, \mu_{\text{Li}}] = E[c] - n_{\text{Li}}[c]\mu_{\text{Li}} \quad (1)$$

where $E[c]$ is the enthalpy, n_{Li} is the lithium concentration of composition c , and μ_{Li} can be any lithium chemical potential. For any given μ_{Li} , the stable structures were found by computing the lower convex hull Φ . The electrochemical stability window is defined as a potential range between which a given compound is stable against decomposition by either Li extraction or Li insertion. The lithium chemical potential μ_{Li} is considered as a function of applied electrostatic potential ΔV [Equation (2)]:

$$\mu_{\text{Li}}(\Phi) = \mu_{\text{Li}}^0 - e\Delta V \quad (2)$$

where μ_{Li}^0 is the chemical potential of Li metal (−1.9089 eV, from DFT) and e is the elementary charge.

Chemical stability

In this study, we consider the interface as a pseudo-binary of two crystalline reactants c_a and c_b . The chemical mixing reaction energy ΔE_{rxn} was determined by minimising the driving force with respect to the mixing ratio x , i.e., by evaluating the x that yielded the most negative reaction driving force [Equation (3)]:^[70]

$$\Delta E_{\text{rxn}} = \min_{x \in [0,1]} \{E_{\text{pd}}[xc_a + (1-x)c_b] - xE[c_a] - (1-x)E[c_b]\} \quad (3)$$

where $E[c_a]$ and $E[c_b]$ are the corresponding convex-hull minimum energies and $E_{\text{pd}}[c]$ is the energy of the ground state structure or phase equilibrium at composition c determined from the phase diagram.

CI-NEB calculations

The single-vacancy migration mechanism of Li-ion diffusion in the candidate coatings was investigated using climbing-image nudged elastic band (CI-NEB) calculations.^[72] The vacancy was created by removing one Li-ion from the pristine structure with a uniform background charge compensating for the missing ion to retain the oxidation state for all ions. An energy cut-off of 520 eV was used, and the forces were converged to within 0.05 eV/Å.

Lithium wettability calculations

The wettability of a coating by metallic Li was evaluated by calculating the work of adhesion W_{ad} at the Li/coating interface using Equation (4):^[73]

$$W_{\text{ad}} = (E_{\text{coating}} + E_{\text{Li}} - E_{\text{int}})/S \quad (4)$$

where S is the interface area, E_{int} is the energy of the Li/coating interface supercell, E_{coating} and E_{Li} refer to the energy of an isolated coating or Li surface slab, respectively. The contact angle θ is calculated based on Young-Dupré equation [Equation (5)]:^[74,75]

$$W_{\text{ad}} = \sigma_{\text{Li}}(1 + \cos\theta) \quad (5)$$

where σ_{Li} is the surface energy of Li metal. The surface energy is determined using Equation (6):

$$\sigma = (E_{\text{slab}} - NE_{\text{bulk}})/2A \quad (6)$$

where A is the surface area, E_{slab} and E_{bulk} refer to the energy of surface slab and bulk structure, respectively. N is the number of bulk structures contained in the surface slab. The interface supercell was assembled from a (001) Li and (001) coating surface slab. Both M-terminating and O-terminating surfaces were considered and only the surface with the lowest surface energy (namely the O-terminating one) was chosen for interface construction. A vacuum layer of at least 10 Å was included. Suitable starting structures were constructed for the interfaces by performing single point calculations of frozen slabs at different separations (see ESI for details), followed by full optimisation of the interface (with the outermost layer of the coating material fixed).

Acknowledgements

C.L. thanks the Chinese Scholarship Council for funding and the UK National Supercomputing Service (Archer 2) for a grant of CPU

time. M.B. acknowledges support by the School of Chemistry and EaStCHEM. Calculations were performed on a local HPC cluster in St Andrews via the EaStCHEM Research Computing Facility, and on Cirrus at EPCC in Edinburgh. We also acknowledge support from The Faraday Institution Grant (FIRG031), New Approaches to processing of oxide solid state batteries. The research data supporting this publication can be accessed at <https://doi.org/10.17630/545b0385-96e7-49af-96b7-a217b4448c6d>.^[76]

Conflict of Interest

The authors declare no conflict of interest.

Data Availability Statement

The research data underpinning this publication can be accessed at <https://doi.org/10.17630/XXX> [DOI to be completed upon acceptance].

Keywords: anode coating • garnet electrolyte • high-throughput screening • Li wettability

- [1] J. B. Goodenough, K. S. Park, *J. Am. Chem. Soc.* **2013**, *135*, 1167.
- [2] A. Manthiram, X. Yu, S. Wang, *Nat. Rev. Mater.* **2017**, *2*, 1.
- [3] C. Wang, K. Fu, S. P. Kammpata, D. W. McOwen, A. J. Samson, L. Zhang, G. T. Hitz, A. M. Nolan, E. D. Wachsman, Y. Mo, V. Thangadurai, L. Hu, *Chem. Rev.* **2020**, *120*, 4257.
- [4] Y. Tian, G. Zeng, A. Rutt, T. Shi, H. Kim, J. Wang, J. Koettgen, Y. Sun, B. Ouyang, T. Chen, Z. Lun, Z. Rong, K. Persson, G. Ceder, *Chem. Rev.* **2021**, *121*, 1623.
- [5] M. Tachez, J. Malugani, R. Mercier, G. Robert, *Solid State Ionics* **1984**, *14*, 181.
- [6] H. Aono, Y. Sugimoto, E. Sadaoka, N. Imanaka, G. Y. Adachi, *J. Electrochem. Soc.* **1990**, *137*, 1023.
- [7] Y. Inaguma, C. Liquan, M. Itoh, T. Nakamura, T. Uchida, H. Ikuta, M. Wakihara, *Solid State Commun.* **1993**, *86*, 689.
- [8] R. Murugan, V. Thangadurai, W. Weppner, *Angew. Chem. Int. Ed.* **2007**, *46*, 7778.
- [9] M. Murayama, R. Kanno, M. Irie, S. Ito, T. Hata, N. Sonoyama, Y. Kawamoto, *J. Solid State Chem.* **2002**, *168*, 140.
- [10] N. Kamaya, K. Homma, Y. Yamakawa, M. Hirayama, R. Kanno, M. Yonemura, T. Kamiyama, Y. Kato, S. Hama, K. Kawamoto, A. Mitsui, *Nat. Mater.* **2011**, *10*, 682.
- [11] A. Hayashi, S. Kama, F. Mizuno, K. Tadanaga, T. Minami, M. Tatsumisago, *Solid State Ionics* **2004**, *175*, 683.
- [12] H.-J. Deiseroth, S.-T. Kong, H. Eckert, J. Vannahme, C. Reiner, T. Zaiß, M. Schlosser, *Angew. Chem.* **2008**, *120*, 767.
- [13] L. Buannic, B. Orayech, J. M. López Del Amo, J. Carrasco, N. A. Katcho, F. Agusse, W. Manalastas, W. Zhang, J. Kilner, A. Llordés, *Chem. Mater.* **2017**, *29*, 1769.
- [14] J. L. Allen, J. Wolfenstine, E. Rangasamy, J. Sakamoto, *J. Power Sources* **2012**, *206*, 315.
- [15] J. F. Wu, W. K. Pang, V. K. Peterson, L. Wei, X. Guo, *ACS Appl. Mater. Interfaces* **2017**, *9*, 12461.
- [16] V. Thangadurai, D. Pinzarlu, S. Narayanan, A. K. Baral, *J. Phys. Chem. Lett.* **2015**, *6*, 292.
- [17] F. Han, Y. Zhu, X. He, Y. Mo, C. Wang, *Adv. Energy Mater.* **2016**, *6*, 1.
- [18] H. Duan, H. Zheng, Y. Zhou, B. Xu, H. Liu, *Solid State Ionics* **2018**, *318*, 45.
- [19] A. J. Samson, K. Hofstetter, S. Bag, V. Thangadurai, *Energy Environ. Sci.* **2019**, *12*, 2957.
- [20] L. Cheng, E. J. Crumlin, W. Chen, R. Qiao, H. Hou, S. Franz Lux, V. Zorba, R. Russo, R. Kostecki, Z. Liu, K. Persson, W. Yang, J. Cabana, T. Richardson, G. Chen, M. Doeff, *Phys. Chem. Chem. Phys.* **2014**, *16*, 18294.
- [21] A. Sharifi, E. Kazyak, A. L. Davis, S. Yu, T. Thompson, D. J. Siegel, N. P. Dasgupta, J. Sakamoto, *Chem. Mater.* **2017**, *29*, 7961.
- [22] H. Huo, Y. Chen, N. Zhao, X. Lin, J. Luo, X. Yang, Y. Liu, X. Guo, X. Sun, *Nano Energy* **2019**, *61*, 119.
- [23] Y. Ruan, Y. Lu, X. Huang, J. Su, C. Sun, J. Jin, Z. Wen, *J. Mater. Chem. A* **2019**, *7*, 14565.
- [24] J. F. Wu, B. W. Pu, D. Wang, S. Q. Shi, N. Zhao, X. Guo, X. Guo, *ACS Appl. Mater. Interfaces* **2019**, *11*, 898.
- [25] Y. Li, X. Chen, A. Dolocan, Z. Cui, S. Xin, L. Xue, H. Xu, K. Park, J. B. Goodenough, *J. Am. Chem. Soc.* **2018**, *140*, 6448.
- [26] K. K. Fu, Y. Gong, B. Liu, Y. Zhu, S. Xu, Y. Yao, W. Luo, C. Wang, S. D. Lacey, J. Dai, Y. Chen, Y. Mo, E. Wachsman, L. Hu, *Sci. Adv.* **2017**, *3*, 1.
- [27] C. L. Tsai, V. Roddatis, C. V. Chandran, Q. Ma, S. Uhlenbruck, M. Bram, P. Heitjans, O. Guillou, *ACS Appl. Mater. Interfaces* **2016**, *8*, 10617.
- [28] W. Feng, X. Dong, P. Li, Y. Wang, Y. Xia, *J. Power Sources* **2019**, *419*, 91.
- [29] J. Duan, L. Huang, T. Wang, Y. Huang, H. Fu, W. Wu, W. Luo, Y. Huang, *Adv. Funct. Mater.* **2020**, *30*, 1.
- [30] W. Luo, Y. Gong, Y. Zhu, Y. Li, Y. Yao, Y. Zhang, K. K. Fu, G. Pastel, C. F. Lin, Y. Mo, E. D. Wachsman, L. Hu, *Adv. Mater.* **2017**, *29*, 1.
- [31] W. Luo, Y. Gong, Y. Zhu, K. K. Fu, J. Dai, S. D. Lacey, C. Wang, B. Liu, X. Han, Y. Mo, E. D. Wachsman, L. Hu, *J. Am. Chem. Soc.* **2016**, *138*, 12258.
- [32] C. Wang, Y. Gong, B. Liu, K. Fu, Y. Yao, E. Hitz, Y. Li, J. Dai, S. Xu, W. Luo, E. D. Wachsman, L. Hu, *Nano Lett.* **2017**, *17*, 565.
- [33] X. Han, Y. Gong, K. Fu, X. He, G. T. Hitz, J. Dai, A. Pearse, B. Liu, H. Wang, G. Rubloff, Y. Mo, V. Thangadurai, E. D. Wachsman, L. Hu, *Nat. Mater.* **2017**, *16*, 572.
- [34] M. Aykol, S. Kim, V. I. Hegde, D. Snydacker, Z. Lu, S. Hao, S. Kirklin, D. Morgan, C. Wolverton, *Nat. Commun.* **2016**, *7*, 1.
- [35] Y. Xiao, L. J. Miara, Y. Wang, G. Ceder, *Joule* **2019**, *3*, 1252.
- [36] A. M. Nolan, E. D. Wachsman, Y. Mo, *Energy Storage Mater.* **2021**, *41*, 571.
- [37] T. Chen, G. Ceder, G. S. Gautam, P. Canepa, *Front. Chem.* **2019**, *7*, 1.
- [38] T. Chen, G. Sai Gautam, P. Canepa, *Chem. Mater.* **2019**, *31*, 8087.
- [39] S. J. Honrao, Y. Yang, B. Radhakrishnan, S. Kuwata, H. Komatsu, A. Ohma, M. Sierhuis, J. W. Lawson, *Sci. Rep.* **2021**, *11*, 1.
- [40] A. Jain, S. P. Ong, G. Hautier, W. Chen, W. D. Richards, S. Dacek, S. Cholia, D. Gunter, D. Skinner, G. Ceder, K. A. Persson, *APL Mater.* **2013**, *1*, 011002.
- [41] S. Yu, H. Park, D. J. Siegel, *ACS Appl. Mater. Interfaces* **2019**, *11*, 36607.
- [42] E. Kazyak, K. H. Chen, A. L. Davis, S. Yu, A. J. Sanchez, J. Lasso, A. R. Bielinski, T. Thompson, J. Sakamoto, D. J. Siegel, N. P. Dasgupta, J. Mater. Chem. A **2018**, *6*, 19425.
- [43] Y. Zhu, X. He, Y. Mo, *J. Mater. Chem. A* **2016**, *4*, 3253.
- [44] S. H. Jung, K. Oh, Y. J. Nam, D. Y. Oh, P. Brüner, K. Kang, Y. S. Jung, *Chem. Mater.* **2018**, *30*, 8190.
- [45] M. D. Tikekar, L. A. Archer, D. L. Koch, *Sci. Adv.* **2016**, *2*, e1600320.
- [46] B. Liu, D. Wang, M. Avdeev, S. Shi, J. Yang, W. Zhang, *ACS Sustainable Chem. Eng.* **2020**, *8*, 948.
- [47] S. Nishimura, "PyAbstantia," can be found under <https://shinichinishimura.github.io/pyabstab/#>, 2017.
- [48] K. Tadanaga, R. Takano, T. Ichinose, S. Mori, A. Hayashi, M. Tatsumisago, *Electrochem. Commun.* **2013**, *33*, 51.
- [49] F. Bianchini, H. Fjellvåg, P. Vajeeston, *Phys. Chem. Chem. Phys.* **2018**, *20*, 9824.
- [50] J. S. Park, X. Meng, J. W. Elam, S. Hao, C. Wolverton, C. Kim, J. Cabana, *Chem. Mater.* **2014**, *26*, 3128.
- [51] R. Xiao, H. Li, L. Chen, *J. Mater.* **2015**, *1*, 325.
- [52] Y. Deng, C. Eames, J. N. Chotard, F. Laleire, V. Seznec, S. Emge, O. Pecher, C. P. Grey, C. Masquelier, M. S. Islam, *J. Am. Chem. Soc.* **2015**, *137*, 9136.
- [53] Y. Liao, P. Singh, K. S. Park, W. Li, J. B. Goodenough, *Electrochim. Acta* **2013**, *102*, 446.
- [54] A. L. Buzlukov, I. Y. Arapova, Y. V. Baklanova, N. I. Medvedeva, T. A. Denisova, S. V. Verkhovskii, *J. Phys. Chem. C* **2016**, *120*, 23911.
- [55] W. Liu, X. Li, D. Xiong, Y. Hao, J. Li, H. Kou, B. Yan, D. Li, S. Lu, A. Koo, K. Adair, X. Sun, *Nano Energy* **2018**, *44*, 111.
- [56] J. Zhou, Q. Wang, M. Zhang, Y. Guo, A. Zhu, X. Qiu, H. Wu, X. Chen, Y. Zhang, *Electrochim. Acta* **2020**, *353*, 1.
- [57] S. Maiti, H. Sclar, R. Sharma, N. Vishkin, M. Fayena-Greenstein, J. Grinblat, M. Taliander, L. Burstein, N. Solomatin, O. Tiurin, Y. Ein-Eli, M. Noked, B. Markovsky, D. Aurbach, *Adv. Funct. Mater.* **2021**, *31*, 1.
- [58] J. chao Zheng, Z. Yang, Z. jiang He, H. Tong, W. jing Yu, J. feng Zhang, *Nano Energy* **2018**, *53*, 613.
- [59] Y. H. Xu, S. X. Zhao, Y. F. Deng, H. Deng, C. W. Nan, *J. Mater.* **2016**, *2*, 265.

- [60] Q. Zhang, W. Jiang, Z. Zhou, S. Wang, X. Guo, S. Zhao, G. Ma, *Solid State Ionics* **2012**, *218*, 31.
- [61] J. Y. Kim, A. Y. Kim, G. Liu, J. Y. Woo, H. Kim, J. K. Lee, *ACS Appl. Mater. Interfaces* **2018**, *10*, 8692.
- [62] Y. Yuan, F. Wu, Y. Liu, X. Wang, K. Zhang, L. Zheng, Z. Wang, Y. Bai, C. Wu, *ACS Appl. Mater. Interfaces* **2020**, *12*, 39362.
- [63] E. Carella, M. T. Hernandez, *Ceram. Int.* **2014**, *40*, 9499.
- [64] T. Hoshino, K. Kato, Y. Natori, M. Nakamura, K. Sasaki, K. Hayashi, T. Terai, K. Tatenuma, *Fusion Eng. Des.* **2009**, *84*, 956.
- [65] T. Hoshino, *Nucl. Mater. Energy* **2016**, *9*, 221.
- [66] G. Kresse, D. Joubert, *Phys. Rev. B: Condens. Matter Mater. Phys.* **1999**, *59*, 1758.
- [67] G. Kresse, J. Furthmüller, *Phys. Rev. B* **1996**, *54*, 11169–111186.
- [68] J. P. Perdew, K. Burke, M. Ernzerhof, *Phys. Rev. Lett.* **1996**, *77*, 3865.
- [69] S. P. Ong, W. D. Richards, A. Jain, G. Hautier, M. Kocher, S. Cholia, D. Gunter, V. L. Chevrier, K. A. Persson, G. Ceder, *Comput. Mater. Sci.* **2013**, *68*, 314.
- [70] W. D. Richards, L. J. Miara, Y. Wang, J. C. Kim, G. Ceder, *Chem. Mater.* **2016**, *28*, 266.
- [71] Y. Zhu, X. He, Y. Mo, *ACS Appl. Mater. Interfaces* **2015**, *7*, 23685.
- [72] G. Henkelman, B. P. Uberuaga, H. Jónsson, *J. Chem. Phys.* **2000**, *113*, 9901.
- [73] Y. Liu, X. S. Ning, *Comput. Mater. Sci.* **2014**, *85*, 193.
- [74] T. Young, *Philos. Trans. R. Soc. London* **1805**, *95*, 65.
- [75] A. Dupré, P. Dupré, *Gauthier-Villars* **1869**.
- [76] C. Liu, H. A. Früchtl, J. T. S. Irvine, M. Bühl, 2022, Computational screening of anode coatings for garnet-type solid-state batteries (dataset). Dataset. University of St Andrews Research Portal. <https://doi.org/10.17630/545b0385-96e7-49af-96b7-a217b4448c6d>.

Manuscript received: November 22, 2021

Revised manuscript received: January 5, 2022

Accepted manuscript online: January 10, 2022

Version of record online: January 27, 2022